In: AIAA SCITECH 2025 Forum. 6-10 January 2025, Orlando, FL, USA. Paper number AIAA
DOI:10.2514/6.2025-2111

Use of Non-intrusive Flow Diagnostics for Aero-engine Inlet Flow Distortion Measurements in an Industrial Wind-tunnel

Tommaso Piovesan[1], Pavlos K Zachos[2] and David G MacManus[3]
Faculty of Engineering and Applied Sciences, Cranfield University, UK

Dirk Michaelis [4]
LaVision GmbH, Göttingen, Germany

Bart van Rooijen [5]
German-Dutch Wind Tunnels, Marknesse, The Netherlands

Christopher Sheaf [6] and Dimitris Arzoglou [7]
Rolls-Royce plc., Derby, UK

In crosswind conditions, aero-engine intakes experience unsteady flow distortions at the fan face, typically caused by the ingestion of ground vortices and flow separation. These distortions can negatively impact both intake performance and the compatibility of the downstream propulsion system. Understanding the aerodynamics of these flows is crucial for developing next-generation aircrafts with propulsion systems integrated more closely with the airframe. Optical measurement techniques provide detailed datasets in both space and time to support this understanding, but several challenges limit their widespread use in propulsion integration testing. This study demonstrates a novel application of non-intrusive flow diagnostics in an industrial setting for propulsion integration testing. Optical measurements were conducted within an aspirated intake configuration and, later, within a fully coupled fan-intake propulsion system representative of a modern high-bypass aero-engine. Several innovative solutions were developed to improve the integration of optical systems into industrial settings and enhance data acquisition efficiency. The analysis of the results yielded significant contributions about the unsteady interactions within civil intakes at crosswind and high incidence conditions, which are expected to have a notable impact on the development of future, closely integrated propulsion systems architectures able to meet the specified NetZero targets.

[1] Doctoral Researcher, Centre for Propulsion and Thermal Power Engineering.
[2] Reader in Propulsion Aerodynamics, Centre for Propulsion and Thermal Power Engineering, AIAA Senior Member.
[3] Professor in Propulsion Aerodynamics, Centre for Propulsion and Thermal Power Engineering, AIAA Member.
[4] Product Manager for Flow Measurement.
[5] Project Manager.
[6] Cold End Centre of Excellence, Installation Aerodynamics Specialist, Rolls-Royce plc.
[7] Cold End Centre of Excellence, Installation Aerodynamics Engineer, Rolls-Royce plc.

© Copyright 2025, Cranfield University, DNW, LaVision GmbH and Rolls-Royce plc. All Rights Reserved.
Published by the American Institute of Aeronautics and Astronautics with permission.

Published by AIAA. This is the Author Accepted Manuscript issued with: Creative Commons Attribution Non-Commercial License (CC:BY:NC 4.0).
The final published version (version of record) is available online at DOI:10.2514/6.2025-2111. Please refer to any applicable publisher terms of use.

Nomenclature

A_∞	=	freestream captured stream tube notional area, m^2
A_{hi}	=	highlight area, m^2
AIP	=	Aerodynamic Interface Plane
D_{hi}	=	highlight diameter, m
D_i	=	intake inner diameter at fan face, m
h	=	vertical distance from lowest point of the highlight plane to ground, m
L	=	intake length, m
$\tilde{\dot{m}}$	=	corrected intake mass flow rate, kg/s
$\dot{m}$	=	intake mass flow rate, kg/s
MFCR	=	Mass Flow Capture Ratio
M_{is}	=	isentropic Mach number
r	=	radius, m
R_i	=	intake inner radius at fan face, m
SC	=	Swirl Coefficient
SI	=	Swirl Intensity, deg
V_∞	=	freestream velocity, m/s
$w, v_\theta, v_r,$	=	cylindrical instantaneous velocities, m/s
x, y, z	=	cartesian frame of reference
α	=	swirl angle, degrees
ρ_∞	=	freestream density, kg/m^3

I. Introduction

Fuel burn reductions and minimizing environmental impact are key drivers in the design of next-generation turbofan engines for civil aviation ([1]-[3]). A key aspect of this development involves re-designing engine installations, with new, ultra-short, and slim nacelle designs proposed to reduce weight and drag. These compact, short engine inlets could replace traditional configurations. However, due to their reduced axial length, such designs may have limited internal diffusion and could interact more significantly with the downstream fan [4] [5]. This makes them more prone to generating complex flow distortion patterns that may negatively affect propulsion system compatibility, particularly under off-design conditions like crosswind. Additionally, the ground vortex created by engine-ground interactions and flow separation on the windward side of the intake introduce further complexities in the flow. The simultaneous presence of these flow features within the intake system can impact the overall aerodynamic and -mechanical performance of the propulsion system. Understanding the aerodynamics of these flows is therefore crucial to designing and integrating fan-intake systems that are more aerodynamically and -mechanically compatible.

The characterization of flows within intake systems under crosswind (Figure 1-left) or high incidence (Figure 1-right) conditions has been extensively investigated previously. Past studies looked at the fundamental formation mechanisms of a ground vortex ([6]-[8]) or its influence on the operating points and geometric parameters of an intake ([9]-[11]). The windward separation was studied in detail across a range of mass flow rates and crosswind velocities by multiple authors ([12]-[16]), whereas, more recently, Murphy et al. [17] and Wang and Gursul [18] focused on the unsteady aspects of the ground vortex in terms of strength and size on measurements planes underneath and in front of the intake. Studies at high angles of attack were also shown by multiple research groups ([19]-[26]). Nevertheless, the swirl distortion caused by the ingested vortex on a nominal Aerodynamic Interface Plane (AIP) inside the intake was never measured before in sufficient spatial or temporal resolution to improve the understanding of the underpinning flow mechanisms. This was partially due to the lack of capability to perform high-resolution measurements within such a confined flow domain, and partially due to insufficient pull-through of such methods into industrial environments where representative engines tests normally take place.

© Copyright 2025, Cranfield University, DNW, LaVision GmbH and Rolls-Royce plc. All Rights Reserved.
Published by the American Institute of Aeronautics and Astronautics with permission.

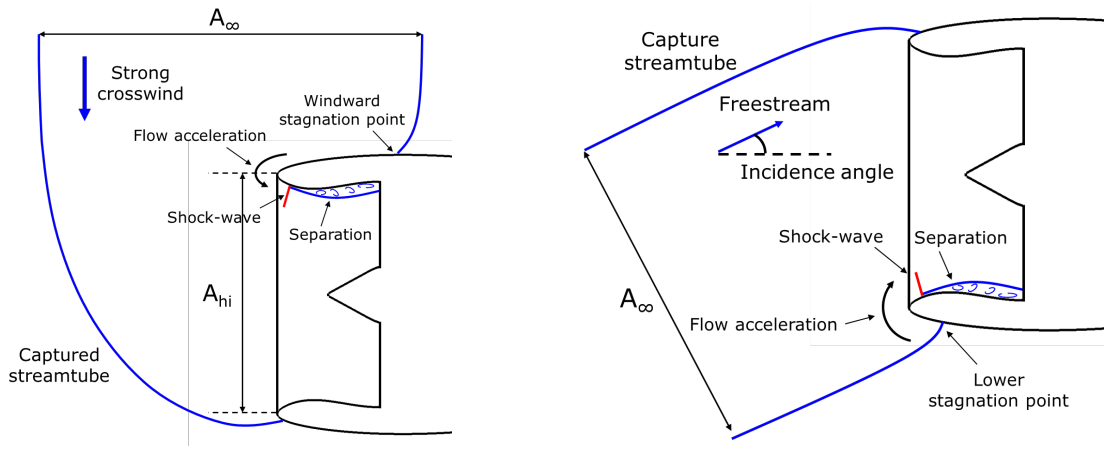


Figure 1 Key flow features within an intake under crosswind (left) and incidence (right) operating conditions.

This paper describes the test campaigns that were undertaken during the CLEAN SKY 2 research programme NIFTI (Non-Intrusive Flow distortion measurements within a Turbofan Intake) with the primary objective to demonstrate the use of non-intrusive distortion measurements in industrial settings for intakes operating at crosswind and high incidence conditions, which is the key novelty of the programme. The programme was coordinated by German-Dutch Wind Tunnels (DNW, The Netherlands), with LaVision GmbH (Germany), Cranfield University (UK) and Imperial College London (UK) as consortium members. Rolls-Royce plc. was the Topic Manager. This new demonstrated ability to characterize unsteady intake flows, substantially improves our understanding about complex intake-fan interactions and can aid the design of future highly closely integrated propulsion architectures. Moreover, the high-resolution data can support numerical tool calibration, validation and verification. These are the main contributions of the work. Finally, use of such data, where possible, by the propulsion integration community can have a significant impact on the re-definition of industrial standards for engine compatibility, which is an acknowledged area where more work is required ([27]-[29]).

II.Aspirated Intake Experiments

A. Test facility, Model and Measurement Setup

The experiments were conducted at the Low-Speed Tunnel of the German-Dutch Wind Tunnels (DNW-LST), which is a continuous, atmospheric wind-tunnel with a 3 m x 2.25 m working section. The maximum achievable tunnel speed (in empty conditions) is 80 m/s. The test setups for the experiments at crosswind and angle of attack are shown in Figure 2 and described in greater detail by Kempaiah et al. [30].

The test article was representative of a modern, very high bypass ratio, scarfed and drooped intake. A conical centerbody was present although the tests were conducted with no fan rotor in place. The hub-to-tip ratio at the notional fan face was 0.3. The vertical distance between the ground plane and the highlight at the intake's bottom dead center (h) was $h/D_{hi} = 0.3$, where D_{hi} is the diameter of the intake highlight plane. The ground plane had an elliptical (2:1) leading edge and spanned the full width of the wind tunnel test section. Transition trips installed at its leading edge were used to ensure fully turbulent flow conditions at the ground plane. The total pressure distribution at the Aerodynamic Interface Plane (AIP) was measured using 8 equi-spaced radial rakes with 10 Pitot probes on each rake (Figure 3-left), with the innermost located at $0.368R_i$ and the outermost at $0.985R_i$, where R_i is the intake inner radius at the notional fan face plane. The rakes at 0º, 90º, 180º and 270º were also instrumented with a total temperature probe, whereas the rakes at 90º and 180º had two additional unsteady pressure sensors for unsteady total pressure measurements. The intake model was equipped with 10 streamwise rows of approximately 18-20 wall static pressure taps each, distributed around the lip at different azimuthal locations, that is 0°, 45°, 67.5°, 90°, 112.5°, 135°, 157.5°, 180°, 202.5°, and 270°.

© Copyright 2025, Cranfield University, DNW, LaVision GmbH and Rolls-Royce plc. All Rights Reserved.
Published by the American Institute of Aeronautics and Astronautics with permission.

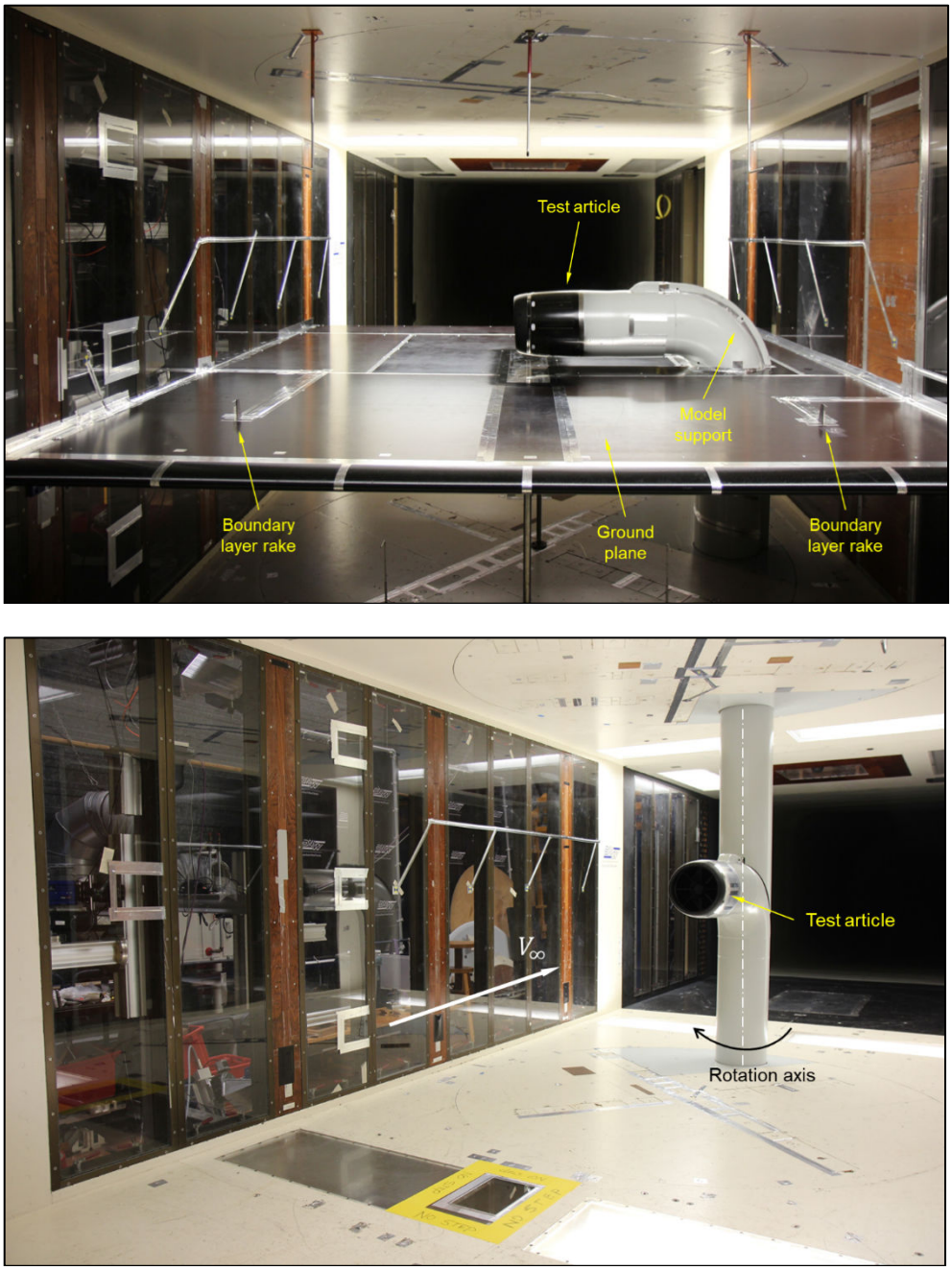


Figure 2 Experimental setups for the crosswind test at DNW-LST. Top: setup for crosswind tests with ground plane. Bottom: setup for angle of attack. Images not to scale [30].

The test article was made to allow for optical, laser-based measurements at the notional fan face. Optical access for the laser sheet was provided via a transparent section embedded within the test model. This enabled crossflow Particle Image Velocimetry (PIV) measurements at two planes separated by $0.04D_i$, where D_i is the intake inner diameter at the notional fan face plane. The PIV plane was illuminated by two (2) Quantel Evergreen Nd:YAG lasers, which were located underneath the wind tunnel floor turntable (Figure 3-right).

© Copyright 2025, Cranfield University, DNW, LaVision GmbH and Rolls-Royce plc. All Rights Reserved.
Published by the American Institute of Aeronautics and Astronautics with permission.

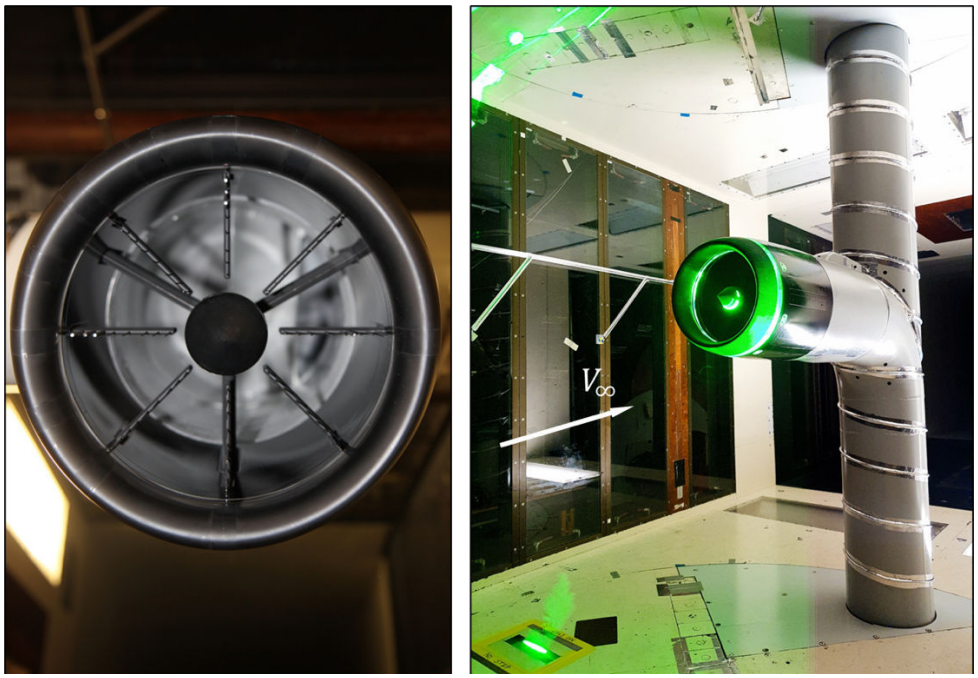


Figure 3 Left: Total pressure rake installed within the test article for total pressure distortion measurement. Right: Test article installed within the DNW-LST at headwind attitude and laser sheet delivered at the notional fan face. Not to scale.

Velocity measurements were taken using a multi-camera set-up consisting of six (6) LaVision Imager sCMOS cameras (2,560 x 2,160 px, 16 bits, 6.5 µm pixel size). Canon lenses with a focal length of 105 mm were used to image the measurement plane. The cameras were positioned outside the test section to avoid interference with the flow through and around the test article (see Kempaiah et al. [30]). Each camera was fitted with an automated, software-driven system that was able to specify pre-determined Scheimpflug and focusing settings for each camera separately to maximize the focus quality and repeatability across the range of model attitudes at incidence, without any requirement for manual adjustment. These prescribed, optimal camera positions for the range of model attitudes were determined during a de-risking pre-experiment and stored in a bespoke software library that was used as a database to retrieve them during the test, based on the required operating condition as shown in [30]. The application of the automated camera positioning method had a significant effect on the productivity of the test campaign. PIV measurements with a velocity field acquisition frequency of 15 Hz were acquired at two (2) crossflow planes within the intake. Another automated traverse enabled the translation of the laser plane between the two prescribed positions during test. Each resulting PIV dataset consisted of a sequence of 1,000 snapshots across a plane of with a diameter of 250 mm. The raw PIV data was processed via LaVision's DaVis 11.0 software. The final achieved spatial resolution was 1.5 mm^2 in both directions across the measurement plane [30].

B. Results and Discussion

The crosswind tests were conducted at a fixed value of mass flow through the intake and across a range of freestream velocities between 2.5 kts (1.3 m/s) and 43 kts (22.1 m/s). The intake's Mass Flow Capture Ratio ($MFCR = \dot{m}/\rho_\infty V_\infty A_{hi}$) was controlled by varying the intake's mass flow rate, which was set as a percentage of a reference maximum value. For the MFCR definition, $\dot{m}$ denotes the intake's mass flow rate, ρ_∞ the free stream density, V_∞ the free stream flow velocity, and A_{hi} the intake's highlight area.

The investigated range of operating conditions is shown in Figure 4 and was previously discussed by Piovesan et al. [31]. For example, optical data acquired for a crosswind velocity of 20 kts (10.3 m/s), indicate that flow separation inside the intake is present for all $MFCR$s across the range from 4.4 to 13.2 (Figure 5). As the MFCR varies, the intake gradually moves from a regime characterized by low-speed separation ($MFCR = 4.4,\ 6.1,\ 7.4,\ 8.8$ and 10.1) to a condition of high-speed separation ($MFCR = 11.2$, 12.5, and 13.2).

© Copyright 2025, Cranfield University, DNW, LaVision GmbH and Rolls-Royce plc. All Rights Reserved.
Published by the American Institute of Aeronautics and Astronautics with permission.

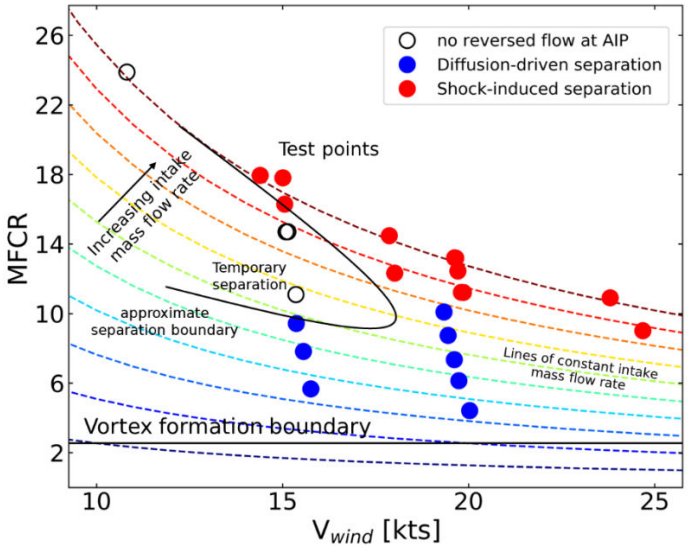


Figure 4 Operating conditions tested during the crosswind campaign at DNW-LST [31].

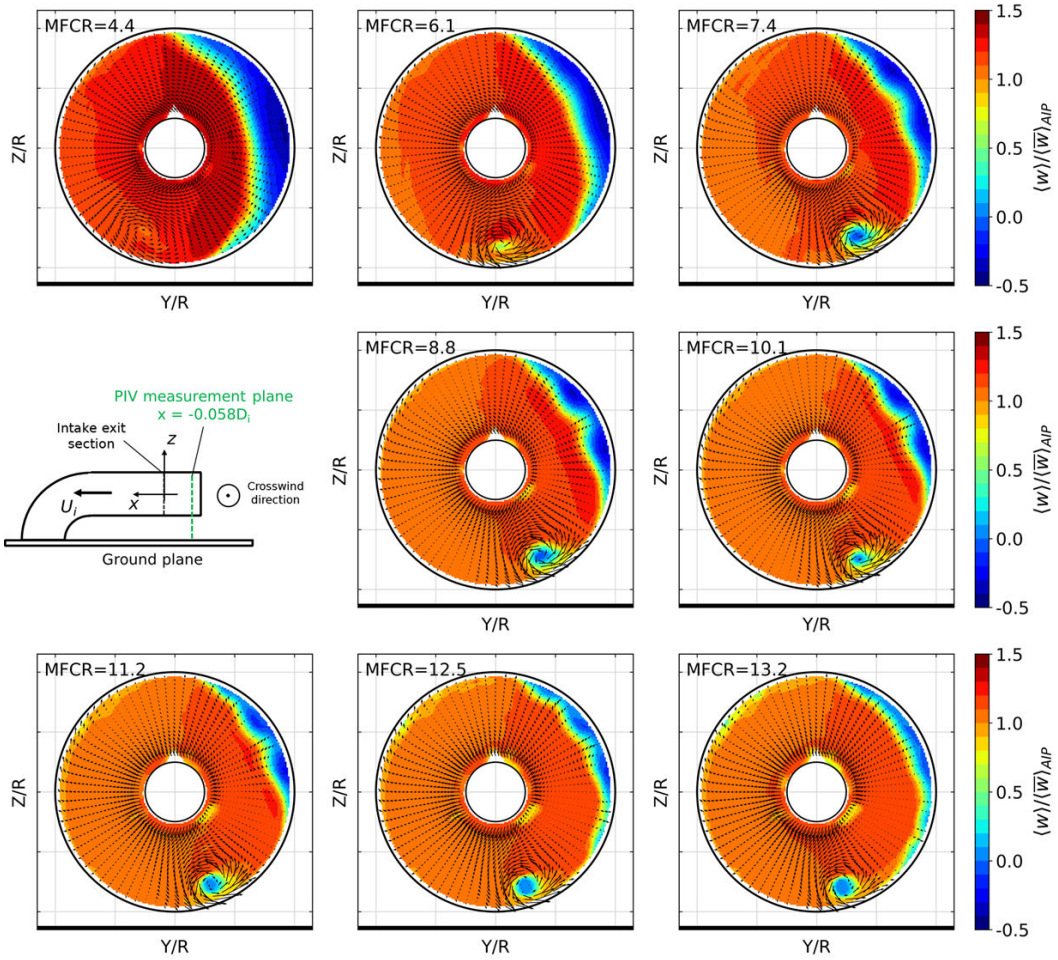


Figure 5 PIV measured time-averaged normalized axial velocity at the AIP with increasing MFCR at a fixed crosswind velocity of 20 kts (10.3 m/s). Crosswind direction from right to left. View looking downstream.

© Copyright 2025, Cranfield University, DNW, LaVision GmbH and Rolls-Royce plc. All Rights Reserved.
Published by the American Institute of Aeronautics and Astronautics with permission.

The aerodynamic behavior of the intake was also investigated for a range of crosswind velocities with the intake mass flow rate set to either the maximum value or 86% of the maximum value, respectively (Figure 4). In these test configurations, for a specified mass flow rate ($\dot{m}$), the $MFCR$ reduces as V_∞ increases (Figure 6). Depending on the combination of $\dot{m}$ and V_∞, the variation in $MFCR$ could result in the intake being attached or separated in either of the two flow regimes. The variation of the normalized axial velocity at the AIP with the crosswind velocity at the maximum mass flow rate through the intake highlights the onset of the separation (Figure 6). In this case, the crosswind velocity varies between 3.5 kts (1.8 m/s) and 30 kts (15.4 m/s) and the corresponding $MFCR$ ranges from 76.8 to 8.8. The intake goes from an attached and mostly uniform regime to a shock-induced flow regime, as indicated by the isentropic Mach number distributions along the intake surface. At low crosswind velocities, nominally 3.5 kts (1.8 m/s) and 6 kts (3.1 m/s), with $MFCR = 76.8$ and $MFCR = 43.4$, respectively, the time-averaged flow around the intake lip is attached and mostly uniform, with no signs of flow separation, apart from a small region of low velocity along the windward side of the intake at $V_\infty = 6$ kts (3.1 m/s). Moreover, for $V_\infty = 3.5$ kts (1.8 m/s) and $V_\infty = 6$ kts (3.1 m/s), the time-averaged axial velocity deficit associated with the ground vortex is barely visible due to the relatively weak vortex, which is also confirmed in the time-average circumferential velocity distributions. As the crosswind velocity increases to $V_\infty = 11$ kts (5.7 m/s and $MFCR = 23.9$), despite no reversed flow in the time-averaged flow field, a wider region of low axial velocity starts to emerge on the upper windward quarter indicating the flow diffusion on the way towards separation. As the crosswind velocity is further increased to $V_\infty = 14$ kts (7.2 m/s and $MFCR = 18.0$) and above, from $V_\infty = 18$ kts (9.3 m/s and $MFCR = 14.5$) to $V_\infty = 30$ kts (15.4 m/s and $MFCR = 8.8$), the intake separates on the windward side, and the size of the distorted region increases, extending from the top dead center to almost the bottom dead center of the intake. Along with a larger area of separated flow, as the crosswind velocity is increased, the size and strength of the ingested ground vortex also increase. In this arrangement with a fixed mass flow rate, Murphy et al. [17] showed that the ground vortex typically increases in strength until it gets close to the blow away $MFCR$ at which point it no longer forms. For this fixed mass flow configuration, the ground vortex idealized blow away $MFCR$ corresponds to a crosswind velocity of 100 kts (around 51 m/s). The azimuthal extent of the windward lip separation does increase with $MFCR$ to the point where at the maximum crosswind velocity of $V_\infty = 30$ kts (15.4 m/s and $MFCR = 8.8$), the two regions of low axial velocity distortion are contiguous.

© Copyright 2025, Cranfield University, DNW, LaVision GmbH and Rolls-Royce plc. All Rights Reserved.
Published by the American Institute of Aeronautics and Astronautics with permission.

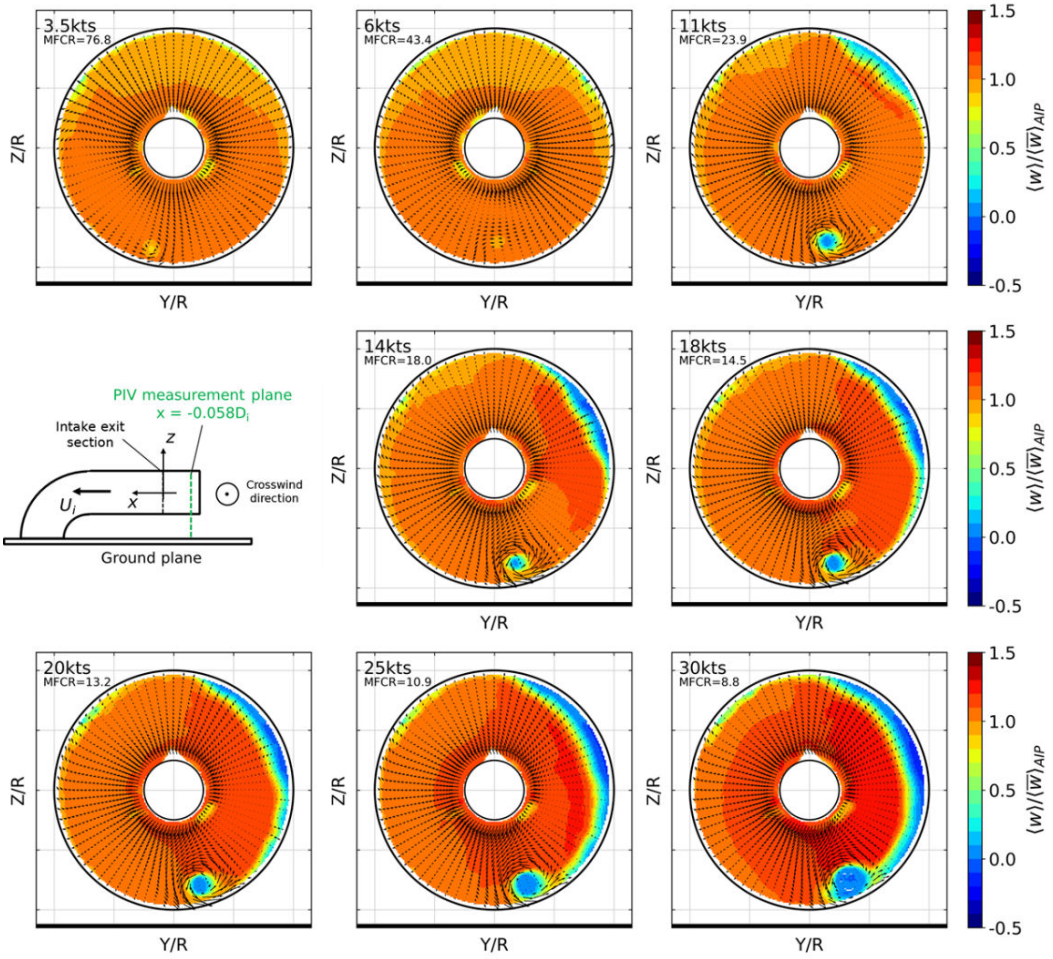


Figure 6 PIV measured time-averaged normalized axial velocity at the AIP with crosswind velocity for a fixed maximum intake mass flow rate. Crosswind direction from right to left. View looking downstream.

The time-averaged swirl angle distributions are shown in Figure 7 for a crosswind velocity of 15 kts (7.7 m/s). For the two attached flow conditions at $MFCR = 11.1$ and 14.7, the distributions of α are primarily dominated by the circumferential velocity and the presence of the ingested ground vortex. For $MFCR = 16.3$ and 17.8, which correspond to shock-induced separation conditions, the extent of the region affected by the ground vortex is reduced, along with the magnitude of the time-averaged swirl angle. In these cases, the separation on the windward side of the intake, apart being responsible of some localized region of high and low values of swirl angle on the upper half of the plane, has only a modest effect on the swirl angle distribution. This is somehow expected, since the region of reversed flow caused by the shock induced separation at the intake lip is localized to the upper part of the AIP and is not very extensive. Of particular interest, are the swirl angle distributions for $MFCR = 5.7$, 7.8, and 9.4, which are characterized by a diffusion-driven separation. The time-averaged α distributions are notably different to the ones at $MFCR = 16.3$ and 17.8 with a much larger region of high swirl angles, both positive and negative, roughly matching the extents of the reversed flow region. Since the corresponding time-averaged circumferential velocity distributions do not show significant levels of circumferential velocity around the region encompassed by the separation, the swirl angle in the upper part of the AIP is therefore mainly due to the axial velocity deficits.

© Copyright 2025, Cranfield University, DNW, LaVision GmbH and Rolls-Royce plc. All Rights Reserved.
Published by the American Institute of Aeronautics and Astronautics with permission.

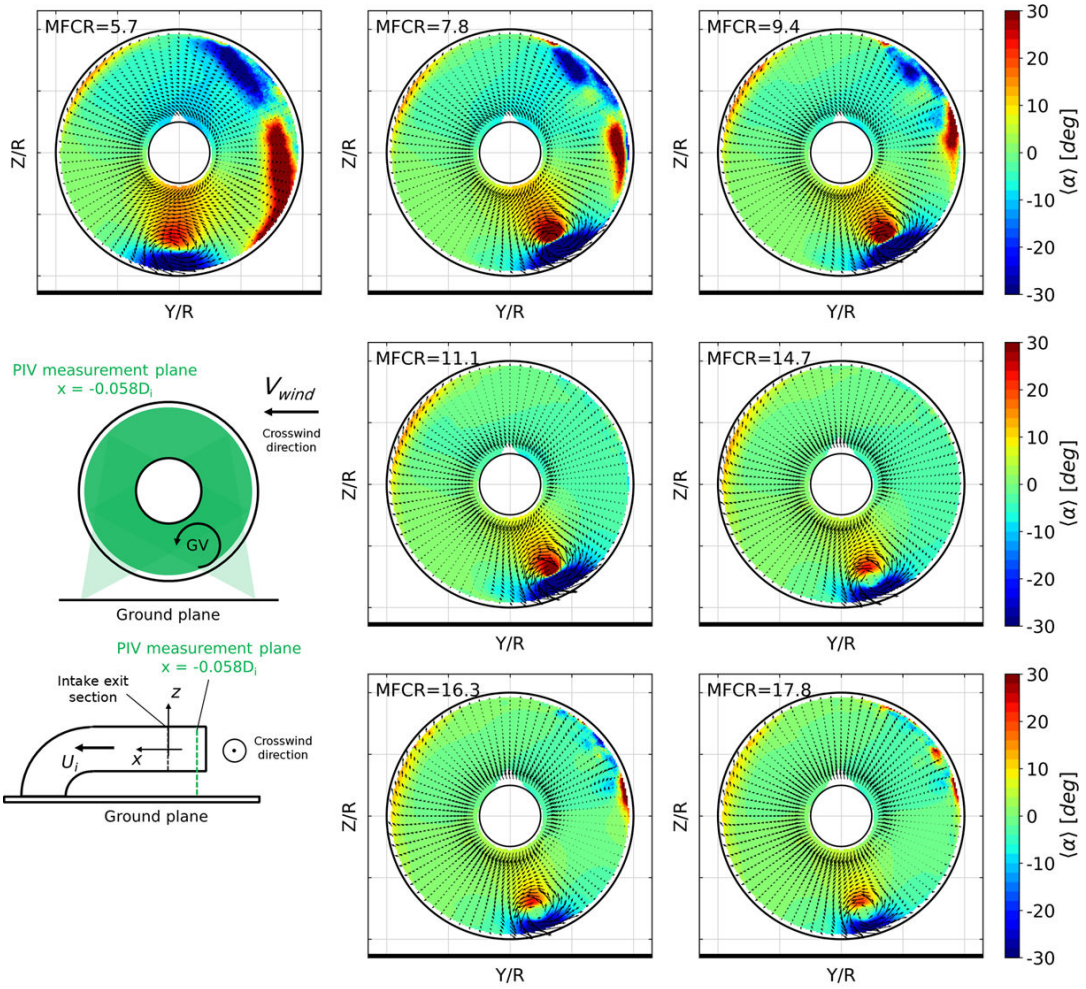


Figure 7 Time-averaged swirl angle distributions at the AIP for increasing Mass Flow Capture Ratio (MFCR) at 15 kts (7.7 m/s). Crosswind direction from right to left. View looking downstream.

The fluctuations of the swirl angle, σ_α, with increasing $MFCR$ are shown in Figure 8. The high swirl regions characterized by high levels of unsteadiness are localized around the ground vortex core, especially at low $MFCR$ (from $MFCR = 5.7$ to 11.1), and in the separation in the top-half of the intake, when present (from $MFCR = 5.7$ to 9.4 and from $MFCR = 16.3$ to 17.8). While the values across the rest of the AIP remain relatively low, the large region of reversed flow introduces high peaks of swirl angle unsteadiness, indicative of large spatial and temporal variations that are greater than the time-averaged values.

© Copyright 2025, Cranfield University, DNW, LaVision GmbH and Rolls-Royce plc. All Rights Reserved.
Published by the American Institute of Aeronautics and Astronautics with permission.

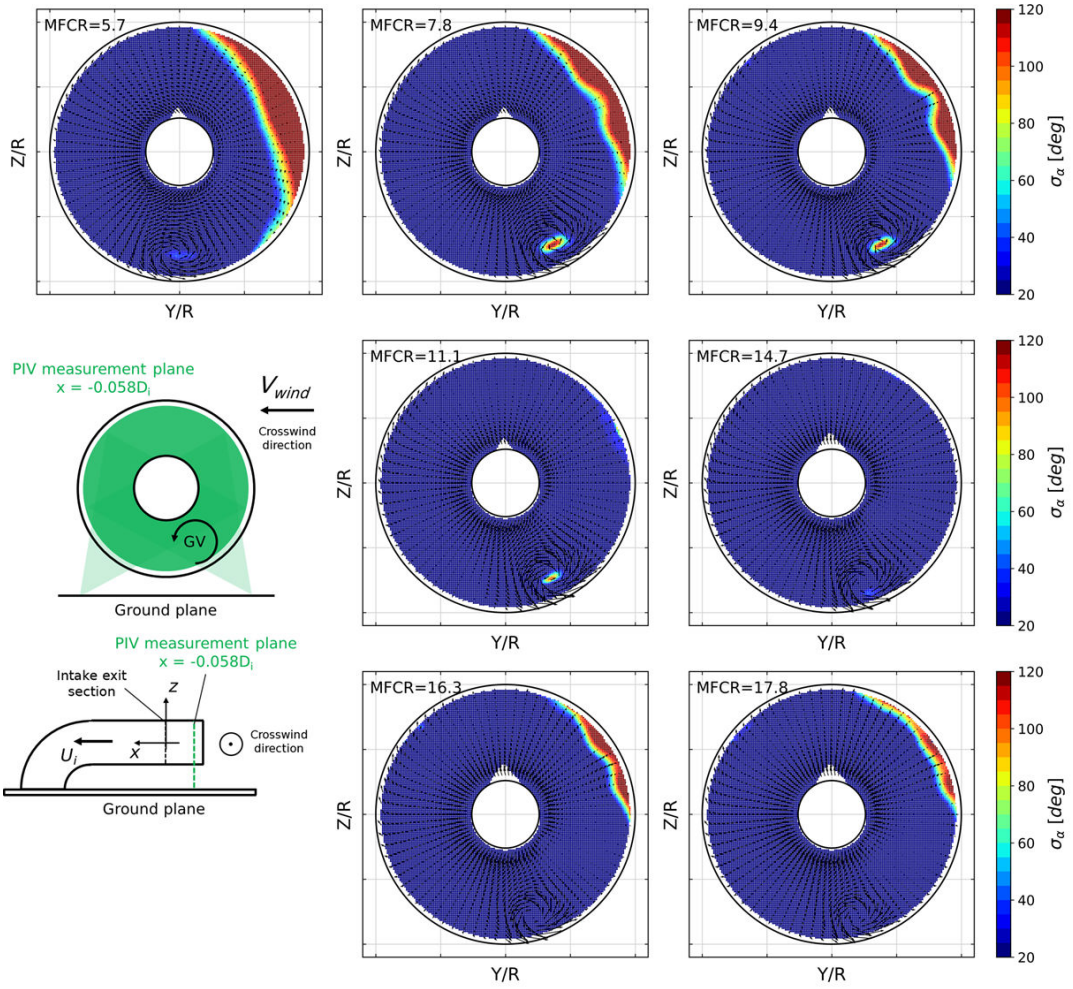


Figure 8 AIP distributions of the swirl angle fluctuations with increasing Mass Flow Capture Ratio (MFCR) for a fixed crosswind velocity of 15 kts (7.7 m/s). Crosswind direction from right to left. View looking downstream.

In previous experimental studies, the focus of the analysis of the ground vortex (GV) was on the determination of its the unsteady characteristics either on a plane underneath the intake [17] or on a plane ahead of the intake [18]. The unique aspect of these experiments enables a quantitative assessment of the GV characteristics across the AIP ahead of the fan face. A first assessment of the unsteady ground vortex behavior was previously presented by Kempaiah et al. [30] for a dataset at a fixed crosswind velocity of 15 kts (7.7 m/s). In this past work it was established that for high MFCR, the ingested vortex oscillates within a narrower area, suggesting a decreasing level of unsteadiness in the vortex core location across the plane. For a higher crosswind speed of 20 kts (10.3 m/s), the instantaneous locations of the ingested ground vortex core are shown in Figure 9 as a function of MFCR. The time-averaged vortex center is indicated by the black marker, while the colors represent the probability, intended as the frequency of occurrence expressed as a percentage of the population, of the ingested vortex to be located at each point on the plane. With increasing $MFCR$, the single anticlockwise vortex increases in strength and moves azimuthally towards the windward side of the intake (Figure 9). Previous investigations ([17] [18]) showed that, for a fixed intake mass flow and increasing crosswind velocity, the ground vortex underneath the intake and at the inlet entrance is highly unsteady and the level of unsteadiness increases as the $MFCR$ decreases. Across the range of $MFCR$ from 4.4 to 10.1, the radial position of the ingested ground vortex core does not change notably, being confined in a region between 0.6 and $0.9R_i$. As $MFCR$ increases, the time-averaged and the instantaneous azimuthal positions reduce from about a θ of 210° to 150° as the ground vortex moves towards the windward side. At the lowest $MFCR$ of 4.4, the vortex moves around on the plane with a relatively wide circumferential area around the time averaged location, with corresponding low

© Copyright 2025, Cranfield University, DNW, LaVision GmbH and Rolls-Royce plc. All Rights Reserved.
Published by the American Institute of Aeronautics and Astronautics with permission.

values of probability, indicating a high level of unsteadiness. The azimuthal variation of the ground vortex position in this case is about 60°. As the $MFCR$ increases to 6.1 and 7.4 this azimuthal variation in vortex position reduces to about 40° and then further to about 20° for $MFCR = 8.8$ and 10.1. As the $MFCR$ is increased from 4.4 to 10.1, the levels of probability associated with the instantaneous ground vortex core location increase, suggesting a decrease in the amount of unsteadiness.

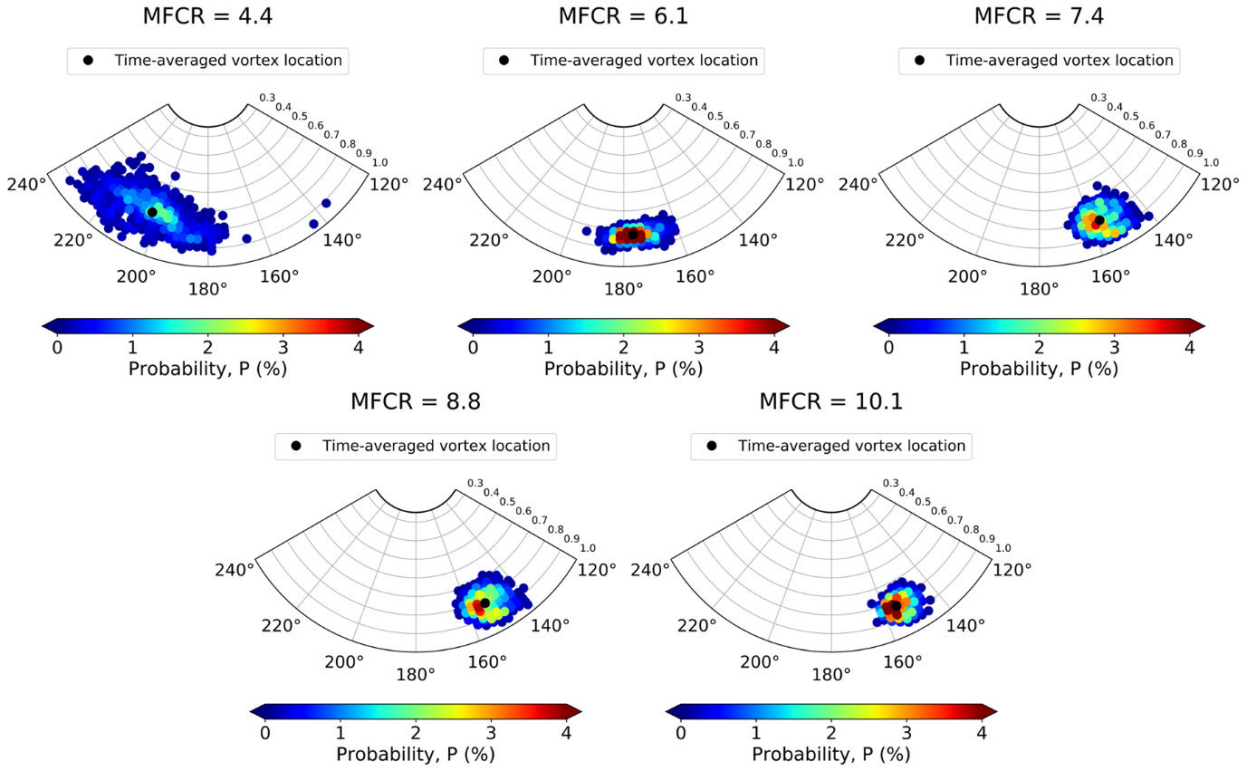


Figure 9 Distribution of instantaneous ground vortex locations at the AIP as a function of Mass Flow Capture Ratio (MFCR) for a fixed crosswind velocity of 20 kts (10.3 m/s).

A key aspect in the assessment of the intake performance is the quantification of the unsteadiness of the separated flow fields around the time-averaged values. A consequential element in the analysis is the evaluation of the swirl distortion linked to the unsteadiness in the axial velocity and the swirl angle fields, to correlate the levels of distortion to the mechanisms of the separation. Distortion analysis was previously shown in the form of unsteady distortion heat maps where pairs of SAE distortion descriptors were represented as described in [32]. These maps proposed the use of a joint Probability Density Function (join-PDF) to quantify the probability to identify a distortion pattern with a certain combination of swirl descriptors (see [32] for a more detailed definition). For example, distributions of swirl coefficient (SC60) versus instantaneous, area-averaged Swirl Intensity (SI) are shown in Figure 10 across a range of MFCR. The signature of the unsteady swirl descriptors depends on the $MFCR$ and the nature of the separation. Across the shown range, the time-averaged and maximum swirl intensity is higher for the case where the diffusion-driven separation is present ($MFCR = 5.7$, Figure 10a), with respect to the time-averaged attached case ($MFCR = 11.1$, Figure 10b) and the case characterized by the shock-induced separation ($MFCR = 16.3$, Figure 10c). Of note are the characteristics of the case at MFCR=11.1. The time averaged flow field was found to be attached, and the swirl descriptors are considerably reduced compared with the case at $MFCR = 5.7$. However, there are some isolated peak distortion events due to the instabilities associated with the instances of the flow in the intake being momentarily separated. This was discussed in detail by Piovesan et al. [31] and clearly demonstrates that separation can generate significant distortion peaks that impact intake performance, leading to distortion events that differ substantially from the time-averaged values, specifically, in this case, twice the average value.

© Copyright 2025, Cranfield University, DNW, LaVision GmbH and Rolls-Royce plc. All Rights Reserved.
Published by the American Institute of Aeronautics and Astronautics with permission.

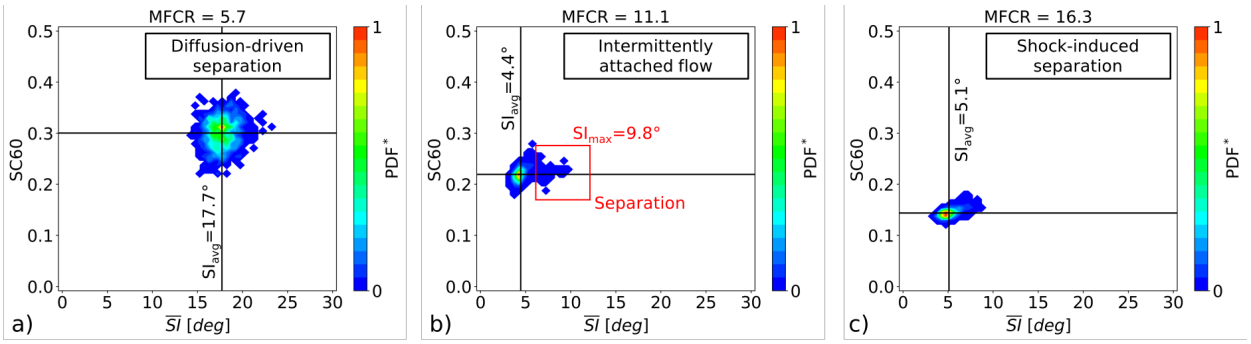


Figure 10 $SC60$-$\overline{SI}$ j-PDF distributions at the AIP: a) $MFCR = 5.7$; b) $MFCR = 11.1$; c) $MFCR = 16.3$ for a fixed crosswind velocity of 15 kts (7.7 m/s).

Finally, as part of the programme, non-intrusive total pressure distortion was calculated via the reconstruction of total pressure AIP distributions using the velocimetry data. Potentially successful calculation of total pressure distortion metrics from velocimetry data would challenge the necessity of intrusive distortion measurement requirements and would enhance the productivity of engine development programmes by providing synchronous, high-resolution, unsteady measurements of swirl and total pressure distortions. Previous work conducted using computational data (Zachos et al. [33]) indicated that it is possible to successfully reconstruct total pressure flow distributions using the underpinning velocity field and a suitable static pressure boundary condition around the measurement plane via the integration of Poisson's Pressure Equation (PPE) across an appropriately discretized domain. This past work also examined the impact of the temporal and out-of-plane velocity gradients on the accuracy of the pressure reconstruction as well as the boundary condition requirements and found that unsteady total pressure flow fields could be reconstructed with reasonable accuracy even without using these temporal or out-of-plane terms.

Total pressure AIP measurements were acquired as part of the NIFTI-LST experiments across the specified test matrix using 8 rakes with 10 total pressure probes each (setup shown in Figure 3-left). These time-averaged AIP total pressure distributions were used to partially validate a PPE based reconstruction of the AIP total pressure distribution using the PIV data. As the optical measurements were conducted across a crossflow plane within the intake and using non-time-accurate PIV acquisition, neither the out-of-plane nor the temporal velocity derivatives were available to the PPE solver. For the pressure reconstruction, time-averaged static pressures were measured at the outer casing and approximately at the same stream-wise location as the PIV plane, and were imposed as boundary condition around the outer boundary. An additional boundary condition was used on the inner boundary to enable the numerical solution of the elliptical set of equations, corresponding to the surface of the centerbody. This inner boundary was treated using a Dirichlet approach, by imposing the pressure distribution measured from the 8 taps located on the centerbody surface.

Measured and reconstructed total pressure fields are shown in Figure 11 across a range of MFCR for a fixed crosswind velocity of 15 kts (7.7 m/s). Pressure field reconstructions were conducted using the PIV velocity distributions, which were initially spatially down sampled to match the pressure rake resolution (80 points across the plane arranged in 8 circumferential rakes with 10 radial probes each). These reconstructions are shown in Figure 11d, e and f for the range of MFCR, in comparison to the measured total pressure distributions (Figure 11a, b and c). For the MFCR=7.4 case, the PPE reconstructed total pressure (Figure 11d) indicates a lower total pressure deficit area on the windward side of the intake compared to the measure distribution (Figure 11a). For the higher MFCR cases with MFCR=14.2 and 17.3 respectively, the PPE based total pressure reconstructed flow fields are generally in better agreement with the measured pressure data (Figure 11e and f). Additional total pressure reconstructions were conducted exploiting the high spatial resolution of the acquired PIV data arranged in 180 azimuthal rakes with 49 radial probes each. These higher resolution reconstructions were able to capture the total pressure field around the ground vortex. This is a key flow feature which is not present neither in the low-resolution rake measurements, nor in the reconstructed pressure profiles using the coarser velocity distribution. Moreover, for the low MFCR=7.4 case, the high-resolution reconstruction shows a pressure deficit region with extent very similar to the one suggested by the PIV based AIP velocity distribution (Figure 7 and Figure 8). This observation reinforces a previous finding that low resolution, intrusive distortion characterizations frequently provide incomplete and potentially misleading information, which can reflect on the subsequent engine development, integration and certification programmes.

© Copyright 2025, Cranfield University, DNW, LaVision GmbH and Rolls-Royce plc. All Rights Reserved.
Published by the American Institute of Aeronautics and Astronautics with permission.

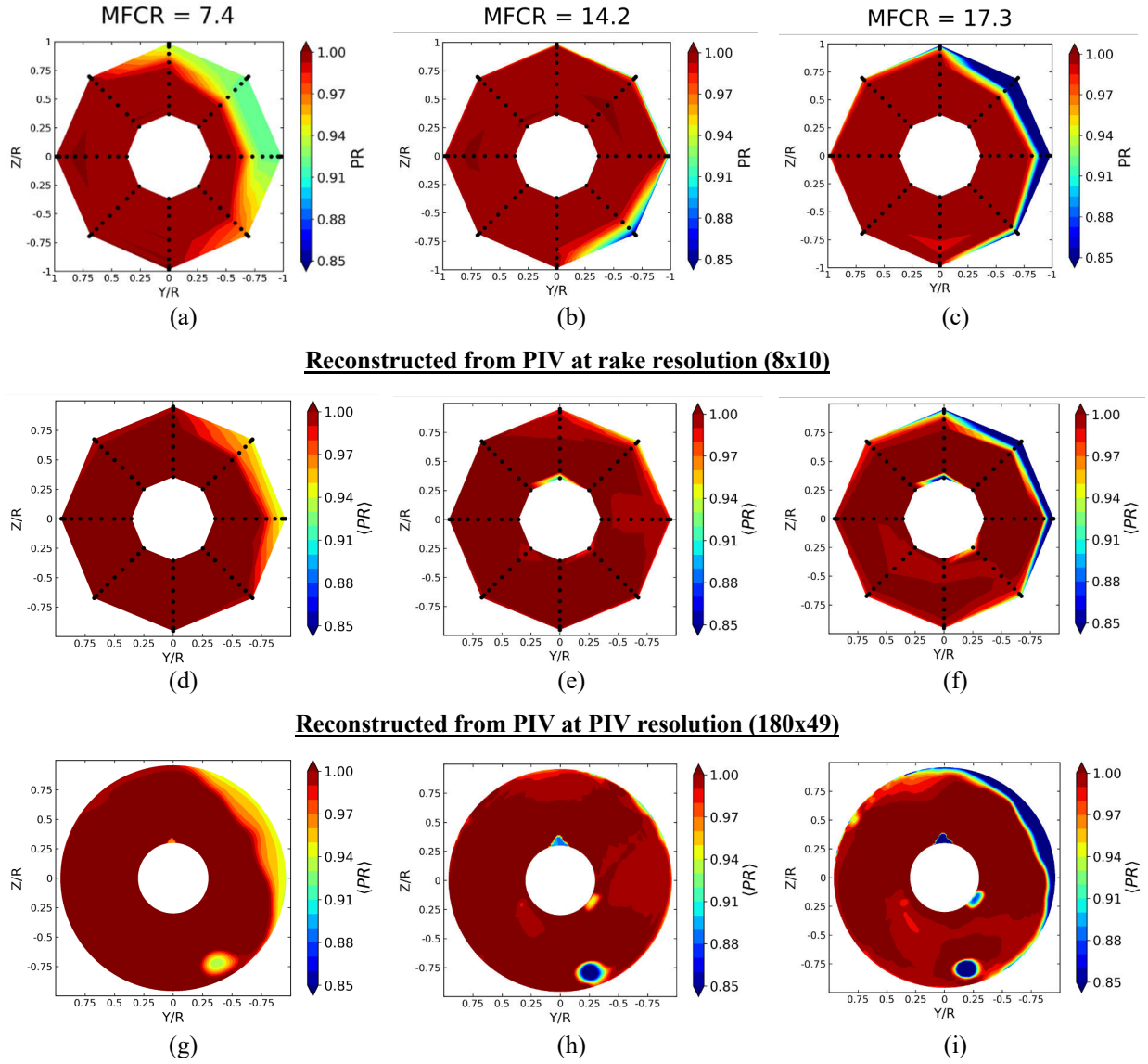


Figure 11 Measured and reconstructed time-averaged total pressure ratio distributions for the case at 15 kts (7.7 m/s). View looking downstream.

Finally, as part of the aspirated intake experiments at DNW-LST, angle of attack (AoA) tests were performed with a freestream Mach number of 0.2 across a range of AoA between 25°-35° with a step of 1° and with the mass flow through the intake set to its nominal design value ($\dot{m}/\dot{m}_{max} = 1.0$). A second AoA sweep was conducted for a lower intake mass flow $\dot{m}/\dot{m}_{max} = 0.9$. Indicative flow field distributions for AoA test points were previously presented by Kempaiah et al. [30].

© Copyright 2025, Cranfield University, DNW, LaVision GmbH and Rolls-Royce plc. All Rights Reserved.
Published by the American Institute of Aeronautics and Astronautics with permission.

III.Coupled Fan-Intake Experiments

A. Test facility, Model and Measurement Setup

Following the optical experiments within the aspirated intake configuration, a subsequent test campaign was caried out within a coupled fan-intake configuration with the aim to provide optical crossflow flow fields across a measurement plane ahead of the fan face under crosswind conditions. These experiments were conducted at DNW's Large Low-speed Facility (DNW-LLF) configured as an open jet with a working section cross-section of 6x6 m^2. The test article included the intake of a generic high bypass ratio civil turbofan aero engine. The aero-line definition of the intake was the sideline of the through flow nacelle from the NASA Common Research Model (CRM), which was previously documented by Vassberg et al. [34]. This model had an axisymmetric intake with no droop or scarf and with a length to highlight diameter ratio L/D_{hi} = 0.425. The intake highlight diameter of this model was 275 mm. The model was powered by a turbine power simulator (TPS) unit that comprised a single stage fan with a diameter of 260 mm (10.2") at the fan face. The fan had 19 rotor and 25 stator blades and an elliptical spinner, as described by Schnell et al. [35]. The operating point of the fan during the experiments was determined via a rake system installed at the bypass and core exhaust ducts which was able to measure both total temperature and pressure around the annulus. The fan pressure ratio was calculated as the ratio of the time averaged, area averaged total pressure at the exit of the fan over the freestream tunnel total pressure. The total pressure and temperature as well as the static pressure at the exit of the fan were used to calculate the ideal Mach number and velocity at the fan exit nozzle. The corrected fan flow was determined through a discharge coefficient that was established during the fan calibration pre-tests. A ground plane was used for these tests, with a size of approximately 2x2 m^2. The non-dimensional ground clearance was h/D_h=0.3, which is a representative value for modern under-wing engine installations. The ground plane boundary layer was tripped to ensure turbulent flow. The boundary layer profile was measured at a reference position on the ground plane upstream of the intake. For both cases reported herein, ground plane boundary layer had a thickness $\delta \approx 14.5\ mm$ and a shape factor $H \approx 1.2$ suggesting a fully turbulent boundary layer.

To enable the optical measurements, the intake model included two transparent rings that allowed laser illumination of 2 crossflow planes ahead of the fan face. PIV Planes 1 (P1) and 2 (P2) centers were located 40 mm and 30 mm upstream of the fan face, respectively (Figure 13). The measurement plane illumination was provided by x2 Quantel Evergreen dual-pulsed Nd:YAG lasers were used (532 nm, 2x200mJ at 15 Hz) which were located underneath the ground plane. A set of optics converted the laser beams into light sheets which were delivered to the P1 and P2 locations within the intake through an acrylic window in the ground plane from the lower left and lower right side, respectively. This dual laser setup was required to mitigate the shadow zones generated by the fan spinner. The two lasers were installed on a linear traverse that allowed the light sheets to be translated parallel to the engine axis to enable illumination of the P1 and P2 planes. The light sheets were independently aligned within the optical ring of the model and subsequently fine-tuned to optimize the axial overlap. The seeding flow was atomized particles of Di-Ethyl-Hexyl Sebacate (DEHS) which were injected into the tunnel's main air stream via a 2 x 2 m seeding rake installed in the settling chamber. The exact axial location and seeding density were remotely control and optimized during the experiment. For image recording, the same multi-camera, variable-geometry PIV setup was used as for the aspirated tests (LaVision Imager sCMOS cameras 2,560 x 2,160 px, 16 bits, 6.5 µm pixel size). Each camera was installed on a rotation unit with remote control to adjust the planar Scheimpflug angle and focus settings. Four of the cameras were equipped with an additional remote control of a second Scheimpflug axis. The cameras had 300 mm focal length lens to enable imaging from a long stand-off distance. The camera lines of sight were defined in such a way that each part of the measurement plane was imaged by at least two cameras to enable stereoscopic PIV measurements. The six-camera array was installed on a frame which was mounted on an elevated platform located outside of the flow stream, at the starboard side of the test section approximately at the same height as the model. The stand-off distance between the camera array and the measurement plane was approximately 8.0 m. All PIV measurements were conducted in a phase-locked arrangement to account for the fan rotational speed. Consequently, the fan blades were imaged at an approximately fixed azimuthal location across the entire dataset. This helped with the background image subtraction as part of the post-processing method and improved the signal to noise ratio of the PIV data. The optical setup and image post-processing yielded a final PIV spatial resolution of approximately 1.5 mm^2 across the measurement plane for all investigated cases at a temporal frequency of 15 Hz. Each PIV data set comprised 1,000 snapshots, which were used to produce the flow statistics.

© Copyright 2025, Cranfield University, DNW, LaVision GmbH and Rolls-Royce plc. All Rights Reserved.
Published by the American Institute of Aeronautics and Astronautics with permission.

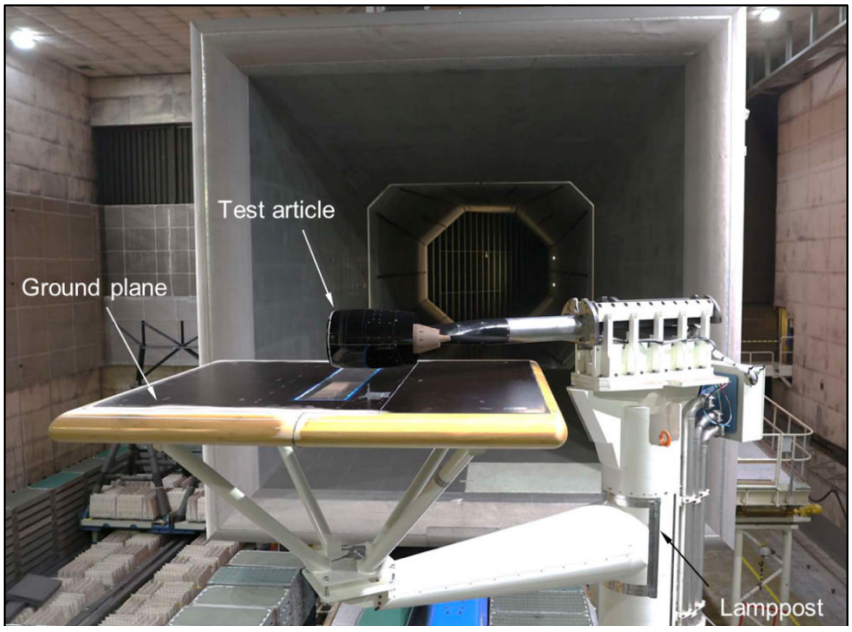


Figure 12 Test article and ground plane installed at DNW-LLF open working section via a lamppost system (view parallel to crosswind direction, looking downstream).

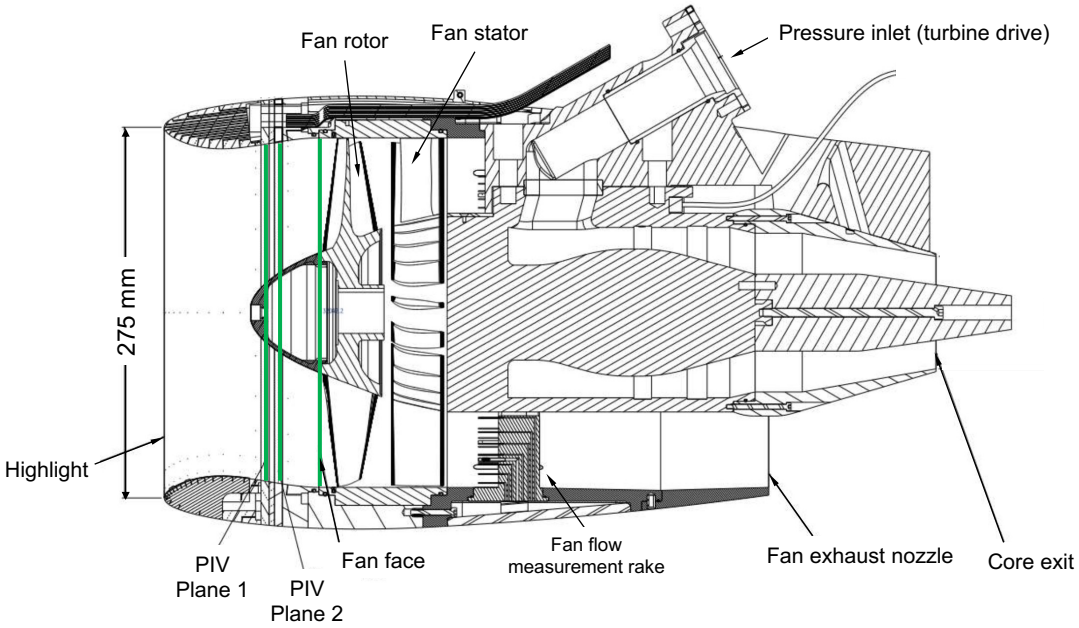


Figure 13 Test article schematic indicating fan face and PIV measurement planes [36].

© Copyright 2025, Cranfield University, DNW, LaVision GmbH and Rolls-Royce plc. All Rights Reserved.
Published by the American Institute of Aeronautics and Astronautics with permission.

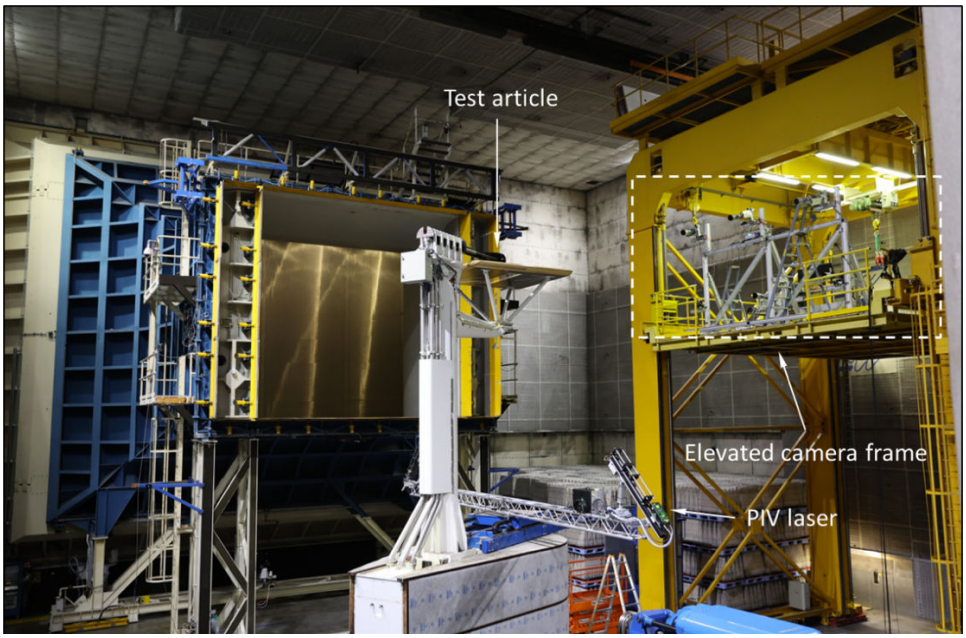


Figure 14 View of the NIFTI-LLF wind tunnel installation indicating the test article in relation to the tunnel's exit nozzle and the location of the PIV camera frame.

B. Results and Discussion

The test conditions ranged between 0 and 30 knots crosswind speeds with TPS rotational speeds between 13,500 and 28,500 RPM in typical steps of approximately 1,500 RPM. These corresponded to ISA-normalized fan flow rates across a range between 4 – 8.3 kg/s and fan pressure ratios between 1.06 to 1.28. The highest fan rotational speed corresponds to a relative to rotor Mach number of 1.05. The PIV velocity fields occupy the measurement plane up to about 96% of its radius. The complete test matrix across the range of crosswind velocities and fan operating points is shown in Figure 15.

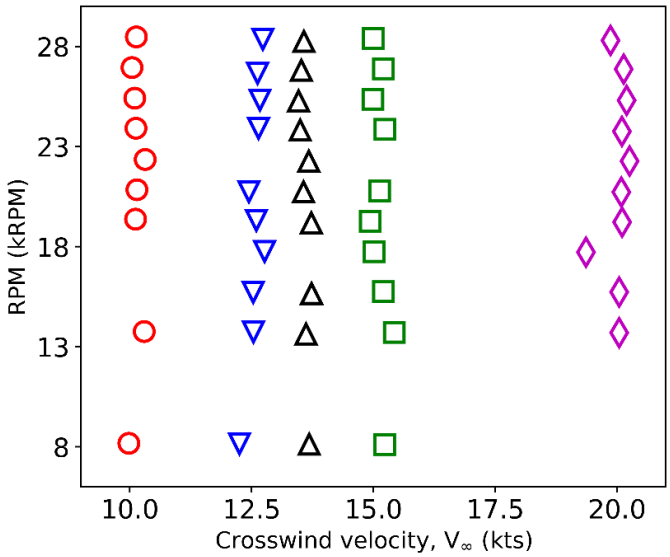


Figure 15 Operating conditions tested during the crosswind campaign at DNW-LLF.

© Copyright 2025, Cranfield University, DNW, LaVision GmbH and Rolls-Royce plc. All Rights Reserved.
Published by the American Institute of Aeronautics and Astronautics with permission.

Instantaneous, normalized, out-of-plane velocity and swirl angle distributions for two representative cases with Mass Flow Capture Ratio ($MFCR = \dot{m}/\rho_\infty V_\infty A_{hi}$) of 17.5 and 8.9 are shown in Figure 16. For MFCR=17.5, the flow at the inner surface of the intake was attached, with the main swirl distortion associated with the ingested ground vortex core also clearly captured at the lower part of the plane. This is evident in the sample snapshots of normalized axial velocity (Figure 16a, b) and swirl angle (Figure 16c, d). The PIV resolution was sufficient to capture the ground vortex core with approximately 30 velocity vectors identified in the general vortex area and about 12 vectors along a line of the vortex core between maximum and minimum circumferential velocity. For a lower fan speed (13.5 krpm) at fixed crosswind velocity of 12.5 knots and MFCR of 8.9, there is a diffusion induced flow separation at the windward inner side of the intake. The signature of the ground vortex is still evident in the axial velocity and swirl angle distributions in lower part of the plane (Figure 16b and d). The instantaneous velocity snapshots were used to compute the time averaged velocity and swirl angle distributions for the two cases (Figure 17). The 1,000 samples were sufficient to produce representative statistics as the standard deviation of the swirl angle varied by less than 1% after approximately 700 samples for both cases [36]. The in-plane velocity vectors are shown on the contour for visualization purposes. The measured flow topologies are broadly aligned with previous measurements at similar operating conditions acquired at the notional fan face within an aspirated intake [30]. For example, the ground vortex position is similar as well as the extent of the separation on the windward lip. Based on previous computational studies, it is expected that the fan rotor would have an influence on the intake's distortion characteristics possibly by improving the flow separation bounds and reducing the levels of inlet flow distortion [37] [38]. However, the presented test case does not allow for quantification of the effect of the rotor as directly comparable data for an aspirated configuration is not available. The time average swirl angle distributions indicate a maximum absolute swirl angle of approximately 30° around the ground vortex and separation regions (Figure 17c and d). For this test arrangement, where the fan rotation is in the anticlockwise direction, this is considered as a co-rotating ground vortex. In the tip region, for the time-averaged data, the swirl from the ground vortex and the separation are both predominately in the anticlockwise direction too which yields negative incidence on the rotor. At a lower blade span, the main effect is due to the inner part of the ground vortex, where there are locally large swirl angles with positive incidence to the rotor for both the attached (MFCR=17.5) and separated (MFCR=8.9) cases. In addition, the ground vortex and separated flow regions are also associated with high levels of unsteadiness. For example, the standard deviation of the swirl angle was over 30° in the ground vortex core region and the separated region for MFCR=8.9 (Figure 18). This suggests that instantaneous, peak swirl distortion events with very high values, and variations, of incidence should be expected locally.

© Copyright 2025, Cranfield University, DNW, LaVision GmbH and Rolls-Royce plc. All Rights Reserved.
Published by the American Institute of Aeronautics and Astronautics with permission.

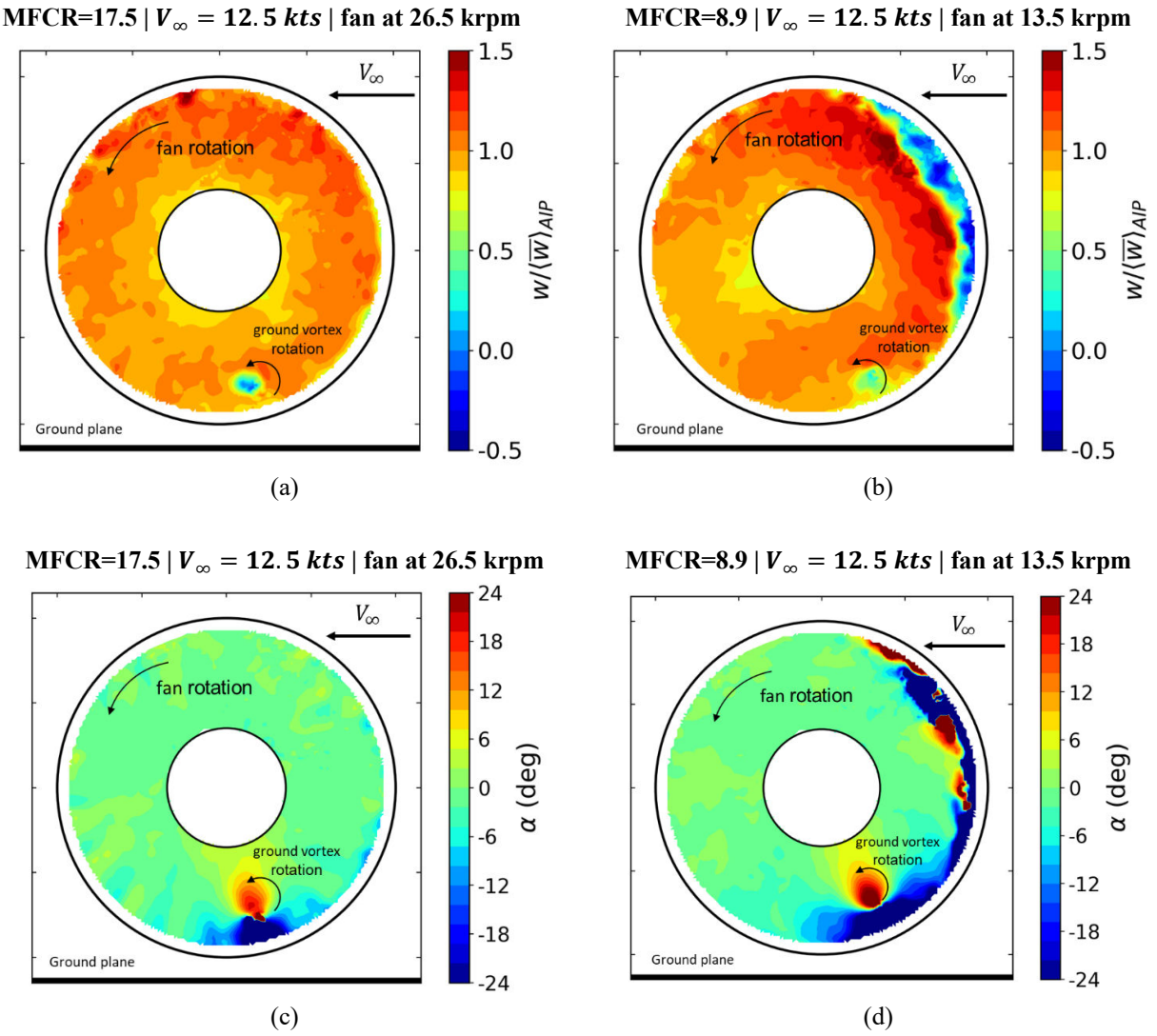


Figure 16 Instantaneous, normalized out-of-plane velocity and swirl angle distributions across PIV Plane 1. View looking downstream.

© Copyright 2025, Cranfield University, DNW, LaVision GmbH and Rolls-Royce plc. All Rights Reserved.
Published by the American Institute of Aeronautics and Astronautics with permission.

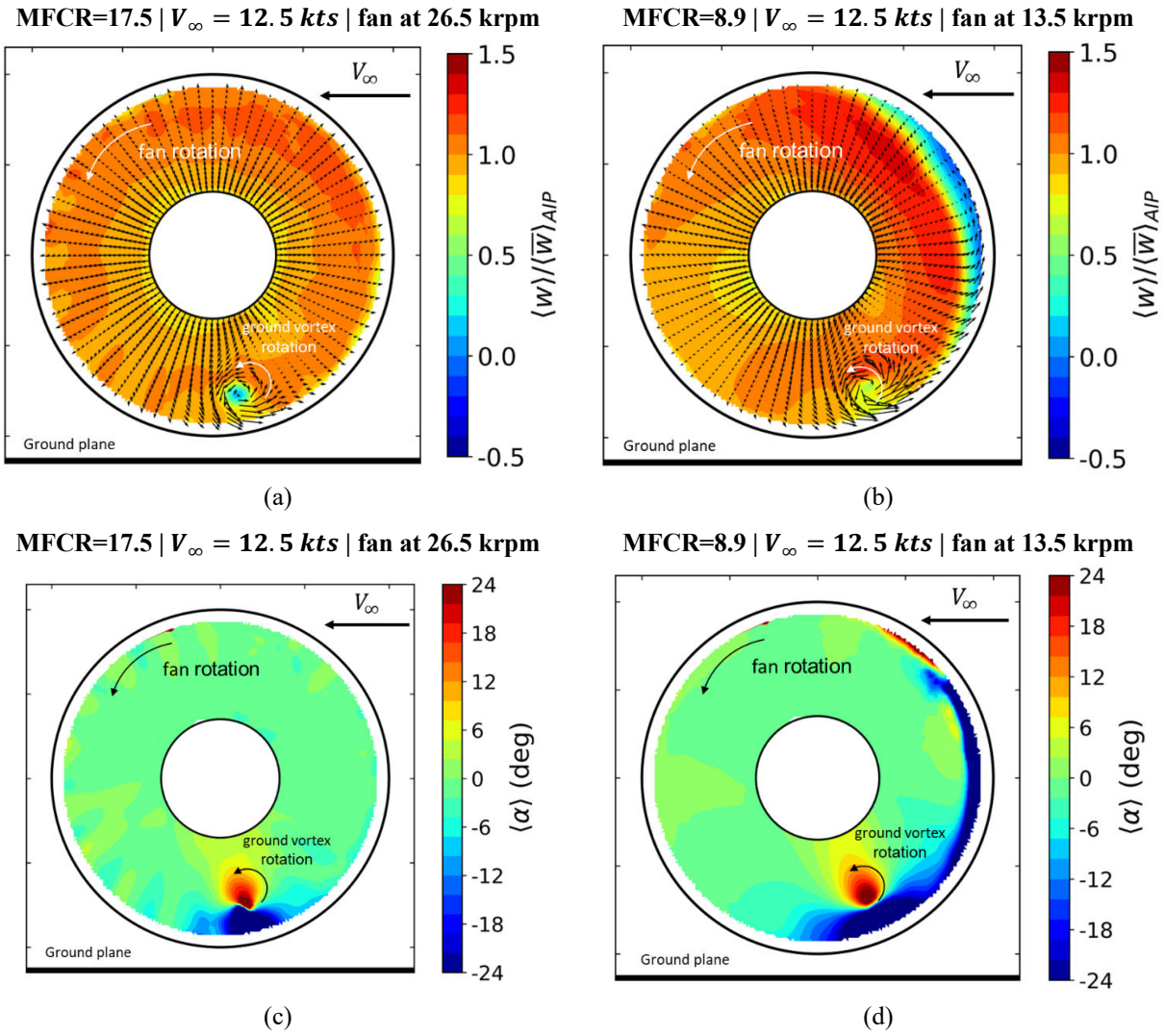


Figure 17 Time-averaged, normalized, out-of-plane velocity and swirl angle distributions across PIV Plane 1. View looking downstream.

© Copyright 2025, Cranfield University, DNW, LaVision GmbH and Rolls-Royce plc. All Rights Reserved.
Published by the American Institute of Aeronautics and Astronautics with permission.

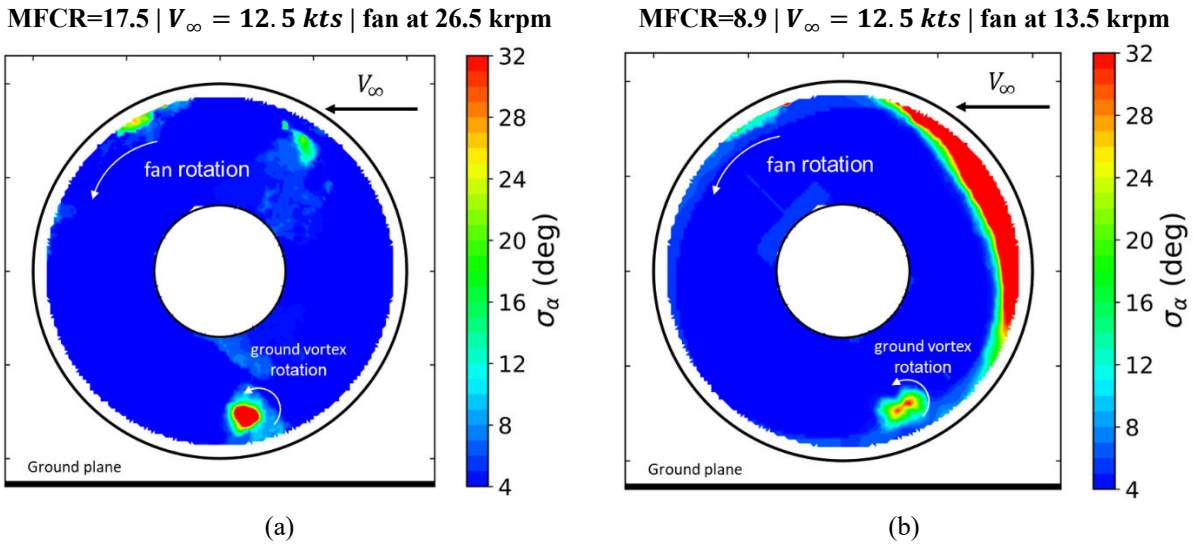
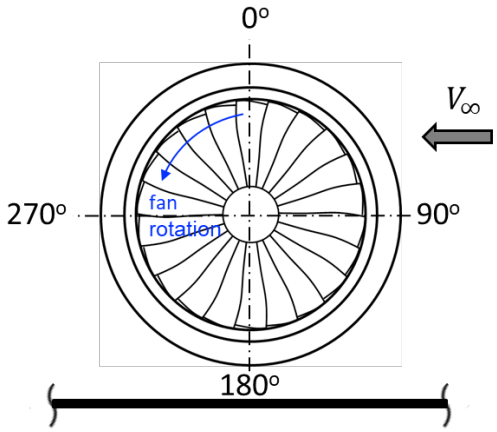


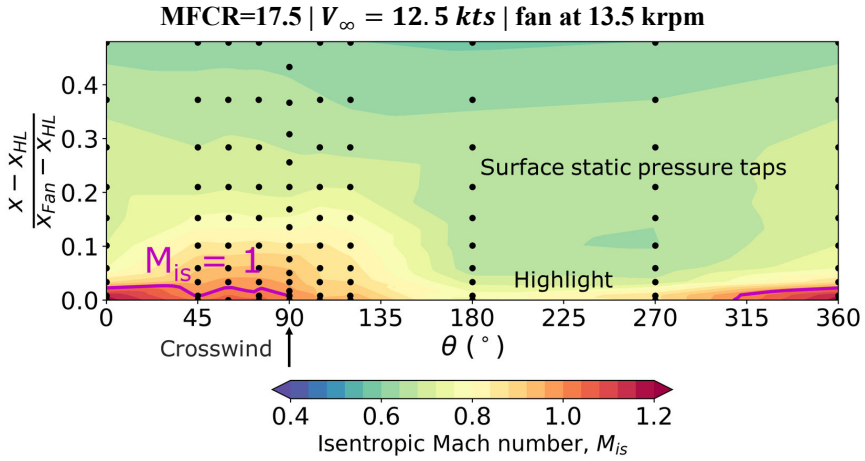
Figure 18 Swirl angle standard deviation across PIV Plane 1. View looking downstream.

As part of the experimentation, lip static pressure data was also recorded across the range of operating conditions. This was used in combination to the optical data to further back up the nature of the observed flow separation. As for the LST experiments, the LLF model intake model was also equipped with 10 streamwise rows of 18-20 wall static pressure taps each, distributed around the lip at different azimuthal locations, that is 0°, 45°, 67.5°, 90°, 112.5°, 135°, 157.5°, 180°, 202.5°, and 270°. Examples of the time-averaged, isentropic Mach number profiles for the two presented operating points are shown in Figure 19, presented as a 2-dimensional plane representing the inner surface of the intake between the highlight plane and the fan face. The black dots indicate the static pressure measurement location, whereas values across the rest of the plane were interpolated from the measured data. For a fixed crosswind velocity (12.5 kts) and MFCR=17.5 (Figure 19b), the isentropic Mach number distribution indicates nearly sonic conditions around the intake lip with no evidence of separation, which is confirmed by the AIP normalized velocity distribution (Figure 17a). For a lower MFCR of 8.9, the isentropic Mach number profile present subsonic peak values all around the intake surface and the separation in this case is diffusion driven (Figure 17b). Further analysis of the remaining operating points of Figure 15 remains work in progress.

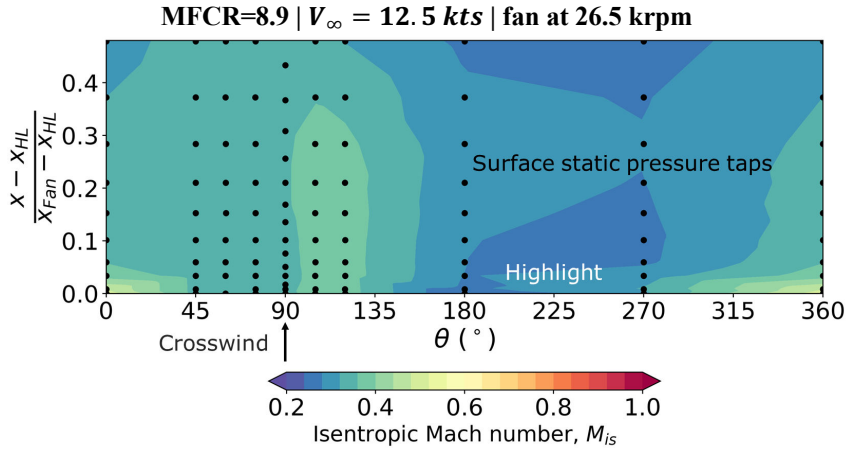
© Copyright 2025, Cranfield University, DNW, LaVision GmbH and Rolls-Royce plc. All Rights Reserved.
Published by the American Institute of Aeronautics and Astronautics with permission.



(a)



(b)



(c)

Figure 19 Time-averaged isentropic Mach number distributions across the inner surface of the intake for a constant crosswind velocity of 12.5 kts and MFCR=17.5 and MFCR=8.9.

© Copyright 2025, Cranfield University, DNW, LaVision GmbH and Rolls-Royce plc. All Rights Reserved.
Published by the American Institute of Aeronautics and Astronautics with permission.

IV. Outlook and Concluding Remarks

The CLEAN SKY 2 NIFTI program successfully demonstrated the use of non-intrusive, laser-based flow diagnostic techniques in industrial settings for propulsion integration measurements. These techniques were able to characterize unsteady distortions ahead of a propulsion system, offering a much more detailed flow description with spatial resolution two orders of magnitude greater than current industry-standard methods, while also significantly reducing costs and testing time. This represents the key novelty of the work, which had not been previously achieved. Several innovative features were developed to facilitate the optical measurements and improve testing productivity. These included a unique multi-camera PIV system with automatic self-calibration that required no user intervention, dual overlapping laser sheets for illumination close to the fan face, innovative optical access through wind tunnel walls, the ground plane, and test article, and effective laser reflection mitigation techniques. Considerable time was also dedicated to pre-testing the optical setup in a more cost-effective environment in an effort to minimize risk prior to entering the industrial wind tunnel.

Tests were conducted on two intake configurations: one aspirated and the other fully coupled to a fan rotor. The test matrix included a range of high incidence angles and crosswind conditions with a ground plane. In addition to the optical velocity data from S-PIV at the fan face, conventional pressure data was collected along the diffuser lip for both configurations, and in the aspirated configuration, AIP pressure measurements were taken to assess total pressure distortions. Results from both test campaigns have been reported in previous papers and are summarized here. The analysis provided several new contributions into the aerodynamics of intakes under crosswind and high incidence conditions—insights that conventional methods could not offer or would only be able to offer at a much higher cost. The developed methods and workflows can accelerate the industrial pull-through of optical methods into industrial settings and aid the design of more integrated fan-intake systems which can benefit from the enhanced knowledge of the complex coupled flow field, than current configurations. These are the key contributions of the programme, which are expected to significantly impact the development of next-generation propulsion systems that meet NetZero targets for future aircraft designs.

Acknowledgments

The work presented herein was conducted under the NIFTI project which received funding from the Clean Sky 2 Joint Undertaking (JU) under Grant Agreement No 864911.

References

[1] Birch, N. T., "2020 Vision: The Prospects for Large Civil Aircraft Propulsion," *The Aeronautical Journal*, Vol. 104, No. 1038, 2000, pp. 347–352. https://doi.org/10.1017/S0001924000063971

[2] Hughes, C., Van Zante, D., and Heidmann, J., "Aircraft Engine Technology for Green Aviation to Reduce Fuel Burn," 2011. https://doi.org/10.2514/6.2011-3531

[3] Owens, R., Hasel, K., and Mapes, D., "Ultra High Bypass Turbofan Technologies for the Twenty-First Century," 1990. https://doi.org/10.2514/6.1990-2397

[4] Boscagli, L., Christie, R., MacManus, D., and Piovesan, T., "Aerodynamics of a Short Intake in Crosswind," *Aerospace Science and Technology*, Vol. 129, 2022, p. 107826. https://doi.org/10.1016/j.ast.2022.107826

[5] Peters, A., Spakovszky, Z. S., Lord, W. K., and Rose, B., "Ultrashort Nacelles for Low Fan Pressure Ratio Propulsors," *Journal of Turbomachinery*, Vol. 137, No. 2, 2015, p. 021001. https://doi.org/10.1115/1.4028235

[6] Siervi, F. De, Viguier, H. C., Greitzer, E. M., and Tan, C. S., "Mechanisms of Inlet-Vortex Formation," *Journal of Fluid Mechanics*, Vol. 124, No. 1, 1982, p. 173. https://doi.org/10.1017/S0022112082002456

[7] Shin, H. W., Cheng, W. K., Greitzer, E. M., and Tan, C. S., "Inlet Vortex Formation Due to Ambient Vorticity Intensification," *AIAA Journal*, Vol. 24, No. 4, 1986, pp. 687–689. https://doi.org/10.2514/3.9330

[8] Shin, H. W., Greitzer, E. M., Cheng, W. K., Tan, C. S., and Shippee, C. L., "Circulation Measurements and Vortical Structure in an Inlet-Vortex Flow Field," *Journal of Fluid Mechanics*, Vol. 162, No. 1, 1986, p. 463. https://doi.org/10.1017/S0022112086002124

[9] Liu, W., Greitzer, E. M., and Tan, C. S., "Surface Static Pressures in an Inlet Vortex Flow Field," *Journal of Engineering for Gas Turbines and Power*, Vol. 107, No. 2, 1985, pp. 387–393. https://doi.org/10.1115/1.3239738

[10] Nakayama, A., and Jones, J. R., "Correlation for Formation of Inlet Vortex," *AIAA Journal*, Vol. 37, No. 4, 1999, pp. 508–510. https://doi.org/10.2514/2.743

[11] Brix, S., Neuwerth, G., and Jacob, D., "The Inlet-Vortex System of Jet Engines Operating near the Ground," 2000. https://doi.org/10.2514/6.2000-3998

[12] Quémard, C., Garçon, F., and Raynal, J., "High Reynolds number air intake tests in the ONERA F1 and S1MA wind tunnels," Workshop on airframe engine integration at DLR, DLR, Mar. 1996, Braunschweig, France.

© Copyright 2025, Cranfield University, DNW, LaVision GmbH and Rolls-Royce plc. All Rights Reserved.
Published by the American Institute of Aeronautics and Astronautics with permission.

[13] Hall, C., and Hynes, T., "Measurements of Intake Separation Hysteresis in a Model Fan and Nacelle Rig," *38th AIAA/ASME/SAE/ASEE Joint Propulsion Conference & Exhibit*, AIAA 2022-3772, 2002. https://doi.org/10.2514/6.2002-3772
[14] Hall, C., and Hynes, T., "Nacelle Interaction with Natural Wind Prior to Take-Off," *38th AIAA/ASME/SAE/ASEE Joint Propulsion Conference & Exhibit*, AIAA 2022-3773, 2002. https://doi.org/10.2514/6.2002-3773
[15] Zhang, M., "Numerical Investigation of Nacelle Intake Flow Distortion at Crosswind Conditions," *32nd Congress of the International Council of the Aeronautical Sciences*, ICAS 2021, 2021, pp. 1–11.
[16] Harjes, L., Bode, C., Grubert, J., Frantzheld, P., Koch, P., and Friedrichs, J., "Investigations of Jet Engine Intake Distortions Caused by Crosswind Conditions," *Journal of the Global Power and Propulsion Society*, Vol. 4, 2020, pp. 48–62. https://doi.org/10.33737/jgpps/118875
[17] Murphy, J. P., and MacManus, D. G., "Ground Vortex Aerodynamics under Crosswind Conditions," *Experiments in Fluids*, Vol. 50, No. 1, 2011, pp. 109–124. https://doi.org/10.1007/s00348-010-0902-4
[18] Wang, Z., and Gursul, I., "Unsteady Characteristics of Inlet Vortices," *Experiments in Fluids*, Vol. 53, No. 4, 2012, pp. 1015–1032. https://doi.org/10.1007/s00348-012-1340-2
[19] Boldman, D., Iek, C., Hwang, D., Larkin, M., and Schweigher, P., "Effect of a Rotating Propeller on the Separation Angle of Attack," 1993. https://doi.org/10.2514/6.1993-17
[20] Motycka, D. L., "Reynolds Number and Fan/Inlet Coupling Effects on Subsonic Transport Inlet Distortion," *Journal of Propulsion and Power*, Vol. 1, No. 3, 1985, pp. 229–234. https://doi.org/10.2514/3.22785
[21] Larkin, M. J., and Schweiger, P. S., "Ultra High Bypass Nacelle Aerodynamics," No. NASA CR-189149, 1992.
[22] Schulze, S., Kähler, C., and Radespiel, R., "On Stalling Flow-Through Nacelles and Powered Inlets at Take-Off Conditions," 2008. https://doi.org/10.2514/6.2008-789
[23] Probst, A., Schulze, S., Radespiel, R., and Kähler, C. J., "Numerical and Experimental Investigation of a Stalling Flow-Through Nacelle," *Notes on Numerical Fluid Mechanics and Multidisciplinary Design*, Vol. 112, 2010, pp. 537–544. https://doi.org/10.1007/978-3-642-14243-7_66
[24] Probst, A., Schulze, S., Kähler, C. J., and Radespiel, R., "Reynolds-Stress Modelling of Subsonic and Transonic Inlet Stall Compared to Measurements," Third Symposium "Simulation of Wing and Nacelle Stall", Braunschweig, 21 - 22 June 2012, pp. 1–13.
[25] Probst, A., Schulze, S., Radespiel, R., and Kähler, C. J., "Numerical Simulation of Engine-Inlet Stall with Advanced Physical Modelling Compared to Validation Experiments," *Notes on Numerical Fluid Mechanics and Multidisciplinary Design*, Vol. 121, 2013, pp. 565–573. https://doi.org/10.1007/978-3-642-35680-3_67
[26] Kennedy, S., Robinson, T., Spence, S., and Richardson, J., "Computational Investigation of Inlet Distortion at High Angles of Attack," *Journal of Aircraft*, Vol. 51, No. 2, 2014, pp. 361–376. https://doi.org/10.2514/1.C031789
[27] "A Methodology for Assessing Inlet Swirl Distortion," Society of Automotive Engineers, SAE International Information Report, SAE Standard 5686, Issued 2010, Reaffirmed March 2022. https://doi.org/10.4271/AIR5686.
[28] Seddon, J., and Goldsmith, E., "Intake Aerodynamics, Second Edition," American Institute of Aeronautics and Astronautics, Inc., Washington, DC, 1999. https://doi.org/10.2514/4.473616
[29] Bouldin, B., and Sheoran, Y., "Inlet Flow Angularity Descriptors Proposed for Use With Gas Turbine Engines," SAE Technical Paper 2002-01-2919, 2002, https://doi.org/10.4271/2002-01-2919.
[30] Kempaiah, K. U., Piovesan, T., Zachos, P. K., Michaelis, D., Gebbink, R., Rooijen, B. van, Gil-Prieto, D., MacManus, D., Sciacchitano, A., and Sheaf, C., "High-Resolution Turbofan Intake Flow Characterization by Automated Stereoscopic-PIV in an Industrial Wind Tunnel Environment," *Measurement Science and Technology*, Vol. 35, No. 2, 2024, p. 025210. https://doi.org/10.1088/1361-6501/ad0ea0
[31] Piovesan, T., Zachos, P. K., MacManus, D. G., and Sheaf, C., "Unsteady Swirl Distortion in a Short Intake Under Crosswind Conditions," *AIAA SCITECH 2024 Forum*, 2024. https://doi.org/10.2514/6.2024-1384
[32] Gil-Prieto, D., MacManus, D. G., Zachos, P. K., and Bautista, A., "Assessment Methods for Unsteady Flow Distortion in Aero-Engine Intakes," *Aerospace Science and Technology*, Vol. 72, 2018, pp. 292–304. https://doi.org/10.1016/j.ast.2017.10.029
[33] Zachos, P. K., Frascella, M., MacManus, D. G., and Gil-Prieto, D., "Pressure Flowfield and Inlet Flow Distortion Metrics Reconstruction from Velocity Data," *AIAA Journal*, 2017, pp. 1–13. https://doi.org/10.2514/1.j055585
[34] Vassberg, J., Dehaan, M., Rivers, M., and Wahls, R., "Development of a Common Research Model for Applied CFD Validation Studies," AIAA 2008-6919, *26th AIAA Applied Aerodynamics Conference*, 2008. https://doi.org/10.2514/6.2008-6919
[35] Schnell, R., Goldhahn, E., and Julian, M., "Design and Performance of a Low Fan-Pressure-Ratio Propulsion System," Proceedings of the 24th International Symposium on Air Breathing Engines 2019 (ISABE 2019), Canberra, Australia, 2019.
[36] Piovesan, T., Zachos, P. K., MacManus, D. G., Kempaiah, K., Michaelis, D., Rooijen, B. van, Vahdati, M., and Sheaf, C., "Coupled Fan-Intake Dynamic Distortion Characterization at Crosswind Conditions," *AIAA Journal*, 2024, pp. 1–5. https://doi.org/10.2514/1.j064595
[37] Mohankumar, B., Hall, C. A., and Wilson, M. J., "Fan Aerodynamics with a Short Intake at High Angle of Attack," *Journal of Turbomachinery*, Vol. 143, No. 5, 2021. https://doi.org/10.1115/1.4050606
[38] MacManus, D. G., and Slaby, M., "Intake Ground Vortex and Computational Modelling of Foreign Object Ingestion," *The Aeronautical Journal*, Vol. 119, No. 1219, 2015, pp. 1123–1145. https://doi.org/10.1017/s0001924000011167

© Copyright 2025, Cranfield University, DNW, LaVision GmbH and Rolls-Royce plc. All Rights Reserved.
Published by the American Institute of Aeronautics and Astronautics with permission.



https://dspace.org/

Use of non-intrusive flow diagnostics for aero-engine inlet flow distortion measurements in an industrial wind-tunnel

Piovesan, Tommaso; Zachos, Pavlos K.; MacManus, David G.; Michaelis, Dirk; van Rooijen, Bart ...

2025-01-06
AIAA
https://doi.org/10.2514/6.2025-2111
Piovesan T, Zachos PK, MacManus D, et al., (2025) Use of non-intrusive flow diagnostics for aero-engine inlet flow distortion measurements in an industrial wind-tunnel. AIAA SCITECH 2025 Forum, 6-10 January 2025, Orlando, FL, USA. Paper number AIAA

Downloaded from a DSpace repository. https://dspace.org/